ARTICLE

Performance and Photovoltaic Response of Polymer-Doped Carbon Nanotube *p*−*n* Diodes

Daner Abdula and Moonsub Shim*

Department of Materials Science and Engineering, University of Illinois at Urbana−Champaign, Urbana, Illinois 61801

ABSTRACT Two terminal abrupt junction diodes are fabricated from single semiconducting carbon nanotubes with simple photopatterned polymer layers defining air-stable *p*- and *n*-regions. These intratube diodes show nearly ideal behavior with relatively low series resistance and no sign of Zener breakdown at room temperature. Spatial doping profiles measured by micro-Raman spectroscopy and selective electrochemical gating of the *n*-region indicate that diode performance depends strongly on relative doping levels. A short circuit current of 1.4 nA with an open circuit voltage of 205 mV are measured when illuminated to saturation.

KEYWORDS: carbon nanotube · diode · *p*−*n* · photovoltaic · Raman spectroscopy

High performance cost-efficient computing, communication, and energy harvesting systems are among many improvements anticipated by incorporating nanoscale materials into electronics and photovoltaics. Because of their unique electronic properties, carbon nanotubes have been at the forefront in the development of next generation electronic devices.[1−4] The *p*−*n* diode is arguably the most pivotal electronic and photovoltaic device. However, theoretical studies have had mixed conclusions on how well a carbon nanotube would perform as the active element in a diode[5,6] with one of the key issues being Zener breakdown caused by small depletion width within the nanotube. Experimentally, this has been averted by implementing an intrinsic region to separate heavily doped regions resulting in a *p*−*i*−*n* structure.[7−10] A major drawback of these *p*−*i*−*n* devices lies in the dual-gate geometry for electrostatic doping which requires cumbersome device fabrication and unnecessarily adds two more terminals to one of the simplest circuit elements. Furthermore, the addition of the intrinsic region degrades device performance by possibly uncovering carrier trap sites (and therefore sometimes requiring further fabrication steps to suspend the active area above the substrate) as well as increasing the series resistance. Chemical doping has been another approach where *p*-doping of nanotubes by ambient air[11−14] is preserved with a polymethylmethacrylate (PMMA) protecting layer over half of the device channel while potassium[15] converts the other half *n*-type.[16] A leaky diode behavior results in this case due to the degenerate doping from such a low work function metal. Such a device also has to be kept under vacuum to maintain the n-doped region. Replacing potassium with small amine molecules can maintain rectifying behavior but only a $p-p^-$ junction has been achieved.[17] Intratube *p*−*n* diodes have also been fabricated using nanotubes partially impregnated with Fe atoms during chemical vapor deposition with ferrocene,[18] but this process lacks the precise spatial control over defining doped regions which may lead to low yields of functional devices.

Here, we fabricate single semiconducting carbon nanotube *p*−*n* diodes by simple patterning of polymers using conventional lithography. Spatial doping modulation is achieved by deep UV lithography of PMMA containing tetracyanoquinodimethane (TCNQ) followed by spin casting polyethylenimine (PEI). Half of the channel covered by PMMA/TCNQ enhances p-type character[19] while the PEI covered region becomes air-stable *n*-type.[20] These devices do not make use of an artificial intrinsic region and are entirely on substrate with a simple two terminal geometry. We show that they are high quality, low-leakage diodes. Doping levels and spatial doping profiles and their effects on diode performance are examined by a combination of Raman and electrochemical gating measurements. Finally, we present our initial studies on photovoltaic response of these intratube *p*−*n* diodes.

*Address correspondence to mshim@illinois.edu.

Received for review June 13, 2008 and accepted September 14, 2008.

Published online September 26, 2008.
10.1021/nn800368s CCC: $40.75

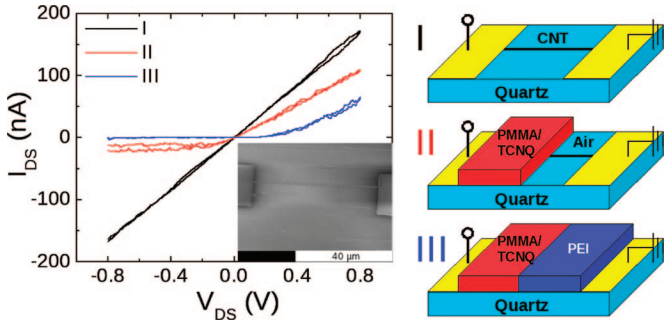

Figure 1. $I_{DS}-V_{DS}$ characteristics at three stages of device fabrication: (I) initial, (II) nanotube protected with PMMA/TCNQ over half the channel and exposed to air on the other half, and (III) completed diode with PEI filling the patterned window. Voltage is always applied on the PMMA/TCNQ side. Both forward and reverse sweeps are shown. Inset is an SEM image of the device in stage I.

RESULTS

Dark Current Characteristics. The progression of $I_{DS}-V_{DS}$ behavior at each step of fabrication for a representative device is shown in Figure 1 along with schematics of the device geometry. After Ar annealing of the as-fabricated device (geometry I), $I_{DS}-V_{DS}$ characteristics are symmetric which ensures that changes in the electrical behavior are due to intentional doping. The onset of current rectification at negative voltages is already achieved in device geometry II even without PEI which indicates that PMMA/TCNQ dopes nanotubes more *p*-type than air, in accordance with the direction of applied bias. After application of PEI, significantly better diode behavior results. Important to note is that we do not see the onset of Zener breakdown as Zhou *et al.*, have[16] with a potassium-doped abrupt p^+-n^+ junction where $I_{DS}-V_{DS}$ becomes nearly ohmic. Our diodes show a reverse current that is 3 orders of magnitude smaller than the forward current when biased at the sweep extrema indicating that we are close to the standard $p-n$ doping profile.

To characterize the performance of the devices, we fit our data to a modified Shockley equation with a series resistance, R_s, similar to Lee *et al.*[8] and Bosnick *et al.*:[10]

$$I_{DS} = I_R\left\{\exp\left[\frac{q(V_{DS} - IR_s)}{nk_BT}\right] - 1\right\} \quad (1)$$

I_R is the ideal diode leakage current, q is the electric charge, and k_BT is the thermal energy. The ideality factor, n, is a measure of carrier generation and recombination from trap sites within the depletion region and takes on values between 1 and 2 with larger values being when trap-mediated generation-recombination current becomes dominant.

Figure 2 shows the fitting results for three devices. A small drawback to using polymers as dopants is their slight conductivity and/or charging which can lead to non-negligible hysteresis at small current levels (see Supporting Information). Because of this hysteresis, we fit only the data in the voltage range where nanotube conductivity is predominant. With the exception of device 2 which contains electrolyte dissolved in PEI, I_{DS} down to a few pA can be analyzed reliably without complications from the hysteresis. Both the forward and the reverse voltage sweeps are shown in Figures 1 and 2 to confirm that the hysteresis does not degrade overall performance.

As the fitting parameters suggest, fabrication of a nearly ideal, on-substrate, two-terminal diode without the intentional use of an intrinsic region is possible. This region has previously been deemed necessary[10] to prevent Zener breakdown[16] due to the small depletion widths expected in abrupt intratube $p-n$ junctions.[5] The absence of this region is expected to decrease R_s and reduce the number of viable defect states that would otherwise increase n. Both devices 1 and 2 show nearly ideal behavior with R_s being only about half of that observed in $p-i-n$ diodes of ref 8 and close to that of $p-i-n$ diodes in ref 10. Note that our diodes have much longer channel lengths (~20 times or more) than devices in refs 8 and 10. Scaled to same lengths, we expect about an order of magnitude improvement in the series resistance. The larger series resistance of device 3 is a consequence of the extent of doping which is explained later.

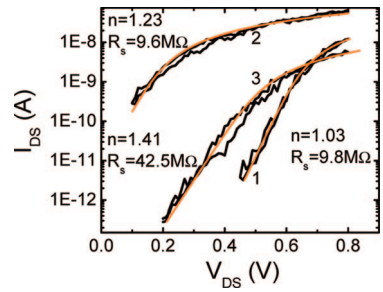

Figure 2. Forward bias current and curve fits for three different devices (labeled 1, 2, and 3) having a range of performance parameters. Device 2 has electrolyte in the PEI defined *n*-region which may be the reason for its higher leakage current. Both forward and reverse sweeps are shown.

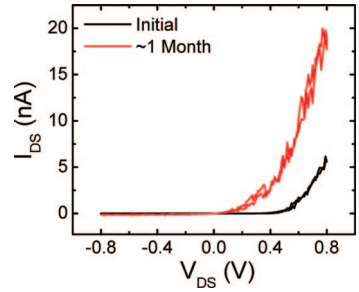

Figure 3. Changes in electrical behavior of device 3 after 1 month in ambient air. Forward and reverse sweeps are shown for both cases.

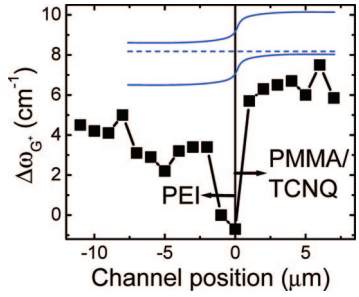

Figure 4. Change in the G-band LO phonon position ($\Delta\omega_{G+}$) of device 2 along the nanotube length around the junction. The vertical line represents the charge neutral point where $E_F = (E_c - E_v)/2$. The inset is a schematic band diagram showing the doping profile of the device according to the observed $\Delta\omega_{G+}$.

In addition to simplicity in fabrication, an advantage of using PEI to achieve *n*-type character is the stability in air. Potassium-doped devices must be kept under vacuum because of the small work function of the alkali metal.[16] Fe-filled carbon nanotube diodes have been shown to be air stable, but the lack of spatial control over doping may lead to low yields of working *p*−*n* junctions.[18] Of the 10 single tube *p*−*n* diodes fabricated by photopatterning of polymers, all have shown rectifying behavior. Figure 3 shows the electrical behavior of diode 3 immediately after fabrication as well as after 1 month in ambient air. The increase in the forward bias current may indicate that the device improves over time, but the reverse current also increases slightly. One probable cause of this may be PEI diffusion into the PMMA/TCNQ region which grades the junction causing I_{DS}−V_{DS} to look increasingly more ohmic. The ability to cross-link PEI[21] can possibly improve stability. Nevertheless, the diode still shows rectifying behavior even after such a long time in air.

Doping Profile and Degree of Doping on Diode Performance. In addition to electrical measurements, Raman spectroscopy has been one of the key approaches to studying charge transfer/doping in carbon nanotubes.[22−26] In the limit of low doping levels, both *p*- and *n*-doping leads to an essentially symmetric upshift in the G-band LO phonon peak positions (ω_{G+}).[27,28] That is, when the Fermi level moves toward either the valence or the conduction band edge, ω_{G+} increases symmetrically from a minimum value $\omega^{(0)}_{G+}$ (which occurs precisely at midgap). A spatial profile of the change in ω_{G+} ($\Delta\omega_{G+}$) around the depletion region of device 2 is shown in Figure 4. Here, $\Delta\omega_{G+}$ = ω_{G+}(geometry III) − ω_{G+}(geometry I), where the device geometries correspond to schematics in Figure 1. Prior to any polymer patterning (geometry I), ω_{G+} is nearly constant at ~1589 cm^{-1} in this region of the nanotube. The charge neutral line is placed where the minimum in $\Delta\omega_{G+}$ appears (i.e., where $\omega^{(0)}_{G+}$ is). At this point $\Delta\omega_{G+} = -1$ cm^{-1} and therefore the initial ω_{G+} is only 1 cm^{-1} higher than $\omega^{(0)}_{G+}$ indicating that this nanotube begins as nearly intrinsic. Upon polymer patterning to define the *p*−*n* junction, there is about 8 cm^{-1} upshift with respect to $\omega^{(0)}_{G+}$ on the PMMA/TCNQ side (*p*-region) indicating that the tube is doped significantly more *p*-type than in air. This difference in doping leads to *p*−*i* junction for the device having geometry II and explains the rectifying behavior even without PEI as observed in Figure 1. The PEI covered side (*n*-region) of the nanotube also exhibits an upshift in ω_{G+} (~5 cm^{-1} with respect to $\omega^{(0)}_{G+}$). Larger $\Delta\omega_{G+}$ on the p-region indicates that the amount of *p*-doping by PMMA/TCNQ is somewhat larger than that of *n*-doping by PEI.

The Raman spectra of *p*- and *n*-regions of all three devices in Figure 2 are shown in Figure 5a. Device 3 which has the lowest performance (*i.e.*, ideality factor n = 1.41 and large series resistance R_s = 42.5 MΩ) exhibits the smallest changes in ω_{G+} with respect to $\omega^{(0)}_{G+}$ (assuming $\omega^{(0)}_{G+}$ to be the same for all three tubes—this assumption is justified given ref 29 where $\omega^{(0)}_{G+}$ has been shown to be independent of diameter for semiconducting tubes). Following ref 27, $\Delta\omega^{n}_{G+}$ ($\Delta\omega^{p}_{G+}$), the G^+ peak spectral shift with respect to $\omega^{(0)}_{G+}$ for the *n*-region (*p*-region), should scale as n_n^3 (p_p^3) in the low doping regime; n_n and p_p are the majority carrier densities. Device 3, then, has the lowest overall doping level with both *p*- and *n*-regions closer to being intrinsic than the other two devices. This leads to a larger series resistance as observed. We also expect less ideal diode behavior for device 3 since low majority carrier density will cause larger depletion widths (W) which in turn leads to larger trap-mediated generation-recombination current (*i.e.*, the trap generation-recombination current is proportional to W, see eq 2 below). According to ref 5, $W \propto \exp(C/\rho)$ for a symmetric *p*−*n* junction ($n_n = p_p \propto \rho$), with doping fraction ρ and constant C. We define an average G^+ peak position shift as $\Delta\tilde{\omega}_{G+} = (\Delta\omega^{n}_{G+} + \Delta\omega^{p}_{G+})/2$ and note $\Delta\tilde{\omega}_{G+} \propto \rho^3$ from the cubic relation described above, leading to $\ln(W) \propto (\Delta\tilde{\omega}_{G+})^{-1/3}$. The decreasing ideality factor n with $\Delta\tilde{\omega}_{G+}$ shown in Figure 5b may then be explained by larger doping levels causing smaller W which in turn decrease trap-mediated generation-recombination current.

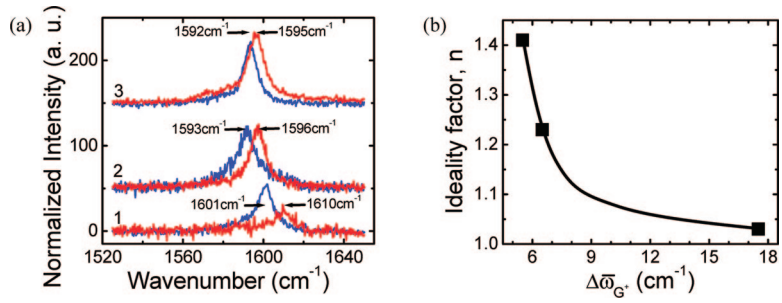

Figure 5. (a) Raman G-band spectra of the *p*-region (red) and *n*-region (blue) of the three diodes from Figure 2. Arrows point to ω_{G+} frequencies at the maxima. (b) Device performance dependence on Raman G^+ peak shift for the same three devices. The ideality factor, n, depends on the degree of doping on each side of the junction, the average of which is represented by $\Delta\tilde{\omega}_{G+}$. The line is a guide to the eye.

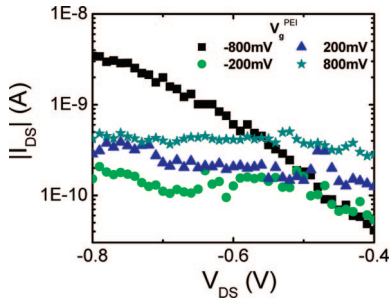

Figure 6. Magnitude of reverse currents for multiple gating potentials on the *n*-region, V_g^{PEI}, as indicated. Hystereses in each curve within the voltage range shown were negligible and the forward and reverse sweeps were averaged for clarity.

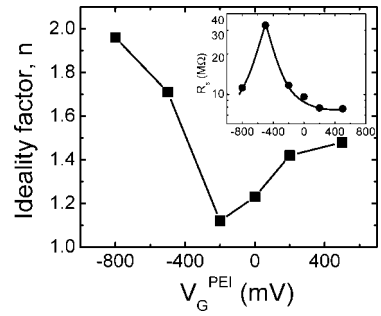

Figure 7. Ideality factor and series resistance (inset) dependences on V_G^{PEI} for device 2. Lines are guides to the eye.

To further investigate the extent of *n*-doping and its effects on device performance, we have electrochemically gated the PEI/electrolyte region of device 2. We first discuss reverse-bias regime. Figure 6 shows the reverse current, I_o, for varying gate potential on the PEI side, V_g^{PEI}. I_o is given by[30]

$$I_o = qA\left(\sqrt{\frac{D_p}{\tau_p}}\frac{n_i^2}{n_n} + \sqrt{\frac{D_n}{\tau_n}}\frac{n_i^2}{p_p} + \frac{n_i W}{\tau_g}\right) \qquad (2)$$

with cross-sectional area *A*, minority carrier diffusion coefficients D_n and D_p, lifetimes τ_p and τ_n, generation lifetime τ_g, and intrinsic carrier concentration n_i. Note that I_o is different from I_R in eq 1 since the third term describing trap-mediated generation current in the depletion region gets incorporated into the ideality factor in eq 1. The first two terms are the ideal reverse-bias saturation current (I_R in eq 1). At constant temperature and bandgap (*i.e.*, constant n_i), increasing the doping level of *n*- or *p*- or both regions should lead to a smaller I_o since n_n and/or p_p will increase and *W* will decrease. However, Figure 6 shows that I_o actually increases with *n*-region doping level (from $V_g^{PEI} = -200$ to $+800$ mV). Different behavior at $V_g^{PEI} = -800$ mV is the expected leaky diode behavior of a $p-i$ (or $p-p^-$) junction. Assuming diffusion coefficients and lifetimes remain constant, the only reason I_o would increase with doping level is if n_i increased. At a fixed temperature, n_i becomes larger only if the band gap becomes smaller. A similar trend of increasing I_o with doping has been observed with the dual-gate diodes and has been attributed to band-gap renormalization (BGR).[9] BGR is the reduction of the band gap at high doping fractions of a semiconductor due to many-body interactions.[31] We can estimate the ratio of reverse-bias saturation currents at two different V_g^{PEI} values V_{g1} and V_{g2} as: $I_o(V_{g1})/I_o(V_{g2}) \approx \exp\{[E_a(V_{g2}) - E_a(V_{g1})]/k_BT\}$ where E_a is the activation energy for minority carrier formation outside of W as described by Lee.[9] Then, we obtain an E_a difference $[E_a(V_{g2}) - E_a(V_{g1})]$ of ~0.02 eV for $V_g^{PEI} = 200$ and 800 mV which is very similar to that seen for dual back-gate voltages of 5 and 7 V reported in ref 9. The smaller gate voltage range needed here is due to the higher efficiency of polymer electrochemical gating.[32,33] These results further support the idea of BGR affecting intratube $p-n$ diode operation.

Figure 7 shows how the series resistance and ideality factor depend on the electrochemical gate potential applied to the *n*-region of device 2. Curve fitting to obtain *n* and R_s is carried out in the same manner as described for devices in Figure 2. The largest value of R_s is seen at $V_G^{PEI} = -500$ mV. We expect the highest resistance when a $p-i$ doping profile is achieved since the "depletion width" is about the size of the entire, highly resistive, intrinsic region. That is, at $V_G^{PEI} = -500$ mV, we completely remove all doping on this side. A Fermi level shift of ~500 mV by PEI doping is consistent with refs 33 and 34. As a more positive V_G^{PEI} increases carrier density in the *n*-region, *W* decreases which in turn decreases R_s as observed. At a more negative gate voltage of -800 mV, the *n*-region is now converted to slightly *p*-type leading again to lower R_s values but at the price of leaky $p-p^-$ junction behavior consistent with the observed reverse current in Figure 6. The PEI/electrolyte gate dependence of *n* shows a minimum value at $V_G^{PEI} = -200$ mV (i.e., about 300 mV above the middle of the band gap inferred from the R_s maximum at -500

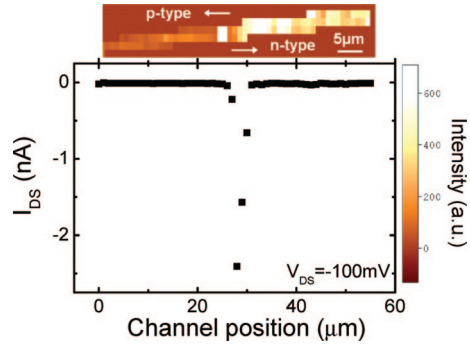

Figure 8. Response of reverse current to 0.44MW/cm² 633 nm excitation for device 2 as the laser (~1 μm spot size) is scanned along the channel of the diode. The Raman intensity spatial map (above) is scaled 1:1 on the position axis of the figure. Lower intensity for the *p*-type region is primarily due to photon scattering through both PEI and the protecting PMMA/TCNQ layer underneath while the laser is only scattered through PEI on the *n*-type side.

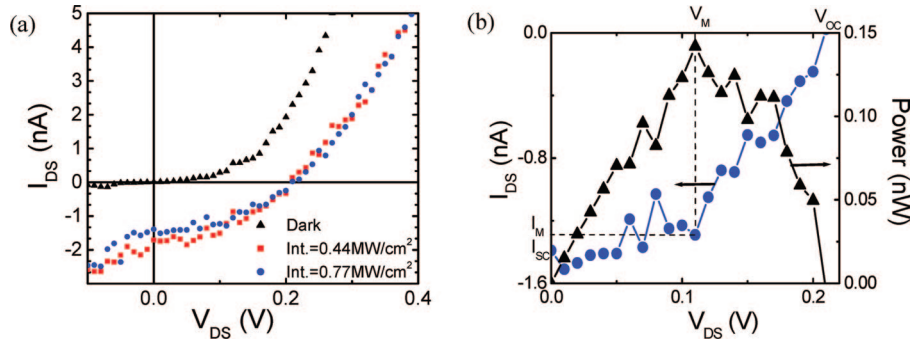

Figure 9. (a) Photovoltaic response of device 2 under laser (633 nm) excitation at the $p-n$ junction. Hysteresis is negligible at this scale and therefore, the forward and reverse sweeps have been averaged for clarity. (b) Close-up of I_{DS} in the power square region for laser intensity 0.77 MW/cm^2 (left axis). Power = $|I_{DS} \times V_{DS}|$ is plotted on the right axis. V_M and I_M are the diode voltage and current values at maximum power. I_{sc} and V_{oc} are short circuit current and open circuit voltage.

mV). As the electrochemical gate potential places the Fermi level at or below the midgap, less ideal diode behavior is expected as $p-i$ or $p-p^-$ junctions are formed and is reflected by the increasing n value for $V_G^{PEI} < -200$ mV. The increasing n for $V_G^{PEI} > -200$ mV may be affected by BGR. The overall gate dependence of n suggests that optimized doping levels may provide ideal behavior even for diodes such as device 3 with large initial n and R_s.

Photovoltaic Response. We now discuss the photovoltaic response of the polymer patterned intratube diodes. The laser from the Raman spectrometer has been used here as the excitation source. This allows a simultaneous measurement of the Raman G-band map (top image in Figure 8) and spatially resolved photoresponse. When the depletion region is excited, the photogenerated electrons and holes are separated by the electric field of the junction which causes an increase in the reverse current. In Figure 8, a sharp increase in the reverse current is seen only at the channel position around 28 μm where the depletion region is located. Photocurrent due to excitation in the doped regions away from the junction is only ~20 pA and is expectedly smaller than reported photocurrent in undoped carbon nanotubes.[35]

The $I_{DS}-V_{DS}$ response to photoexcitation at the diode junction is shown in Figure 9a. An open circuit voltage (V_{oc}) of 205 mV and a short circuit current (I_{sc}) of 1.4 nA are observed at both laser intensities used. In the limit of low photogenerated carrier densities, I_{sc} is expected to scale linearly with the excitation intensity.[8] The same $I_{DS}-V_{DS}$ characteristics at the two intensities indicate that we are in the high intensity (saturation) regime. Although we cannot measure efficiency in this regime, the maximum power and the fill factor for this intratube $p-n$ diode can be determined. The power square region is enlarged for the higher intensity excitation response along with the corresponding power in Figure 9b. The maximum power this nanotube diode can provide is about 0.14 nW. The fill factor of the power square is a measure of how well V_{oc} and I_{sc} translate to power output and is calculated as FF = $(I_M V_M)/I_{sc}V_{oc}$ = 0.498 for this device. While I_{sc} and power cannot be compared directly, FF obtained here is in the upper end of the range reported for suspended dual-gate diodes with similar V_{oc}.[8] Further studies are underway to better quantify photovoltaic properties.

CONCLUSION

We have presented a facile route to nearly ideal two-terminal carbon nanotube diodes that are stable in air. Raman spectroscopy and electrochemical gating measurements have been used to examine how the degree of doping and the doping profile along the length of the nanotube affect diode performance. With optimized doping levels, nearly ideal diode behavior without the need for an intrinsic region has been demonstrated. Initial studies on photovoltaic response presented here indicate that these devices perform comparably to electrostatically dual-gated nanotube diodes[8] without the need for cumbersome fabrication steps to define additional terminals and trenches to suspend the nanotube.

METHODS

Devices were fabricated on preannealed single-crystal AT-cut quartz wafers.[36] Ferritin catalyst (Sigma), diluted 80000× with DI water, was spin cast on the substrates at 2000 rpm for 30 s. Substrates with catalyst deposited were heated in air to 800 °C then placed under Ar/H_2 (150 sccm/150 sccm) flow and heated to 900 °C. Nanotubes were grown with CH_4/H_2 (300 sccm/150 sccm) flow for 15 min at 900 °C. Ti/Au (3 nm/35 nm thick) electrodes with a channel length of ~55 μm were evaporated on lithographically patterned samples (Shipley 1805 resist, MicroChem MF-26A developer). All devices were annealed in 150 sccm Ar flow at 300 °C for 1 h prior to measurements to ensure symmetric $I_{DS}-V_{DS}$ characteristics before $p-n$ junction fabrication. Polymethylmethacrylate (PMMA) with 0.03 wt % tetracyanoquinodimethane (TCNQ) was used to define p-region and neat polyethylenimine (PEI, MW ≈ 25000 daltons, Aldrich) was used for n-region. First, PMMA/TCNQ was spin coated at 3000 rpm for 60 s. Standard deep UV lithography was carried out to open a window over half of the channel. Then PEI was spin cast on the device at 3000 rpm for 2 min. For electrochemical gating measurements, a solution of 30 wt % PEI and $LiClO_4 \cdot 3H_2O$ (4:1 PEI/$LiClO_4 \cdot 3H_2O$ by weight) in methanol was used instead of neat PEI.

Electrical measurements were conducted with an Agilent 4156C semiconductor parameter analyzer. Raman data were collected using a Jobin Yvon LabRam HR 800 micro-Raman with a 633nm laser excitation and a 100× air objective providing a spot size of ~1 μm. Raman signals from polymer films are removed us-

ing background spectra taken where there is no nanotube present. Scanning electron microscope images were obtained on a Hitachi 4700 SEM operating at 1 kV accelerating voltage.

Acknowledgment. This material is based upon work supported by NSF (Grant Nos. CCF-0506660 and DMR-0348585). Scanning electron microscopy was carried out in the Center for Microanalysis of Materials, University of Illinois at Urbana−Champaign, which is partially supported by the U.S. Department of Energy under Grant No. DEFG02-91-ER45439.

Supporting Information Available: Control $I_{DS}-V_{DS}$ characteristics across a device channel covered by PMMA/TCNQ and PEI layers in the absence of a nanotube. This material is available free of charge *via* the Internet at http://pubs.acs.org.

REFERENCES AND NOTES

1. Tans, S. J.; Verschueren, A. R. M.; Dekker, C. Room-Temperature Transistor Based on a Single Carbon Nanotube. *Nature* **1998**, *393*, 49–52.
2. Kong, J.; Franklin, N. R.; Zhou, C.; Chapline, M. G.; Peng, S.; Cho, K.; Dai, H. Nanotube Molecular Wires as Chemical Sensors. *Science* **2000**, *287*, 622–625.
3. Kang, S. J.; Kocabas, C.; Ozel, T.; Shim, M.; Pimparkar, N.; Alam, M. A.; Rotkin, S. V.; Rogers, J. A. High-Performance Electronics using Dense, Perfectly Aligned Arrays of Single-Walled Carbon Nanotubes. *Nat. Nanotechnol.* **2007**, *2*, 230–236.
4. Sazonova, V.; Yaish, Y.; Ustunel, H.; Roundy, D.; Arias, T. A.; McEuen, P. L. A Tunable Carbon Nanotube Electromechanical Oscillator. *Nature* **2004**, *431*, 284–287.
5. Francois, L.; Tersoff, J. Novel Length Scales in Nanotube Devices. *Phys. Rev. Lett.* **1999**, *83*, 5174–5177.
6. Esfarjani, K.; Farajian, A. A.; Hashi, Y.; Kawazoe, Y. Electronic and Transport Properties of *n*−*p* Doped Nanotubes. *Appl. Phys. Lett.* **1999**, *74*, 79–81.
7. Lee, J. U.; Gipp, P. P.; Heller, C. M. Carbon Nanotube *p*−*n* Junction Diodes. *Appl. Phys. Lett.* **2004**, *85*, 145–147.
8. Lee, J. U. Photovoltaic Effect in Ideal Carbon Nanotube Diodes. *Appl. Phys. Lett.* **2005**, *87*, 073101-1−073101-3.
9. Lee, J. U. Band-Gap Renormalization in Carbon Nanotubes: Origin of the Ideal Diode Behavior in Carbon Nanotube *p*−*n* Structures. *Phys. Rev. B* **2007**, *75*, 075409-1−075409-5.
10. Bosnick, K.; Gabor, N.; McEuen, P. Transport in Carbon Nanotube *p*−*i*−*n* Diodes. *Appl. Phys. Lett.* **2006**, *89*, 163121-1–163121-3.
11. Collins, P. G.; Bradley, K.; Ishigami, M.; Zettl, A. Extreme Oxygen Sensitivity of Electronic Properties of Carbon Nanotubes. *Science* **2000**, *287*, 1801–1804.
12. Sumanasekera, G. U.; Adu, C. K. W.; Fang, S.; Eklund, P. C. Effects of Gas Adsorption and Collisions on Electrical Transport in Single-Walled Carbon Nanotubes. *Phys. Rev. Lett.* **2000**, *85*, 1096–1099.
13. Dukovic, G.; White, B. E.; Zhou, Z.; Wang, F.; Jockusch, S.; Steigerwald, M. L.; Heinz, T. F.; Friesner, R. A.; Turro, N. J.; Brus, L. E. Reversible Surface Oxidation and Efficient Luminescence Quenching in Semiconductor Single-Walled Carbon Nanotubes. *J. Am. Chem. Soc.* **2004**, *126*, 15269–15276.
14. Shim, M.; Back, J. H.; Ozel, T.; Kwon, K.-W. Effects of Oxygen on the Electron Transport Properties of Carbon Nanotubes: Ultraviolet Desorption and Thermally Induced Processes. *Phys. Rev. B* **2005**, *71*, 205411-1–205411-9.
15. Lee, R. S.; Kim, H. J.; Fischer, J. E.; Thess, A.; Smalley, R. E. Conductivity Enhancement in Single-Walled Carbon Nanotube Bundles Doped with K and Br. *Nature* **1997**, *388*, 255–257.
16. Zhou, C.; Kong, J.; Yenilmez, E.; Dai, H. Modulated Chemical Doping of Individual Carbon Nanotubes. *Science* **2000**, *290*, 1552–1555.
17. Kong, J.; Dai, H. Full and Modulated Chemical Gating of Individual Carbon Nanotubes by Organic Amine Compounds. *J. Phys. Chem. B* **2001**, *105*, 2890–2893.
18. Li, Y. F.; Hatakeyama, R.; Shishido, J.; Kato, T.; Kaneko, T. Air-Stable *p*−*n* Junction Diodes Based on Single-Walled Carbon Nanotubes Encapsulating Fe Nanoparticles. *Appl. Phys. Lett.* **2007**, *90*, 173127-1–173127-3.
19. Takenobu, T.; Takano, T.; Shiraishi, M.; Murakami, Y.; Ata, M.; Kataura, H.; Achiba, Y.; Iwasa, Y. Stable and Controlled Amphoteric Doping by Encapsulation of Organic Molecules Inside Carbon Nanotubes. *Nat. Mater.* **2003**, *2*, 683–688.
20. Shim, M.; Javey, A.; Kam, N. W. S.; Dai, H. Polymer Functionalization for Air-Stable *n*-Type Carbon Nanotube Field-Effect Transistors. *J. Am. Chem. Soc.* **2001**, *123*, 11512–11513.
21. Kurth, D. G.; Broeker, G. K.; Kubiak, C. P.; Bein, T. Surface Attachment and Stability of Cross-Linked Poly(ethylenimine)-Epoxy Networks on Gold. *Chem. Mater.* **1994**, *6*, 2143–2150.
22. Rao, A. M.; Eklund, P. C.; Bandow, S.; Thess, A.; Smalley, R. E. Evidence for Charge Transfer in Doped Carbon Nanotube Bundles from Raman Scattering. *Nature* **1997**, *388*, 257–259.
23. Kazaoui, S.; Minami, N.; Matsuda, N.; Kataura, H.; Achiba, Y. Electrochemical Tuning of Electronic States in Single-Wall Carbon Nanotubes Studied by *in situ* Absorption Spectroscopy and AC Resistance. *Appl. Phys. Lett.* **2001**, *78*, 3433–3435.
24. Kavan, L.; Rapta, P.; Dunsch, L.; Bronikowski, M. J.; Willis, P.; Smalley, R. E. Electrochemical Tuning of Electronic Structure of Single-Walled Carbon Nanotubes: *In-situ* Raman and Vis-NIR Study. *J. Phys. Chem. B* **2001**, *105*, 10764–10771.
25. Kavan, L.; Dunsch, L. Diameter-Selective Electrochemical Doping of HiPco Single-Walled Carbon Nanotubes. *Nano Lett.* **2003**, *3*, 969–972.
26. Shim, M.; Ozel, T.; Gaur, A.; Wang, C. Insights on Charge Transfer Doping and Intrinsic Phonon Line Shape of Carbon Nanotubes by Simple Polymer Adsorption. *J. Am. Chem. Soc.* **2006**, *128*, 7522–7530.
27. Tsang, J. C.; Freitag, M.; Perebeinos, V.; Liu, J.; Avouris, Ph. Doping and Phonon Renormalization in Carbon Nanotubes. *Nat. Nanotechnol.* **2007**, *2*, 725–730.
28. Das, A.; Sood, A. K.; Govindaraj, A.; Saitta, A. M.; Lazzeri, M.; Mauri, F.; Rao, C. N. R. Doping in Carbon Nanotubes Probed by Raman and Transport Measurements. *Phys. Rev. Lett.* **2007**, *99*, 136803-1–136803-4.
29. Jorio, A.; Souza Filho, A. G.; Dresselhaus, G.; Dresselhaus, M. S.; Swan, A. K.; Ünlü, M. S.; Goldberg, B. B.; Pimenta, M. A.; Hafner, J. H.; Lieber, C. M. *et al.* G-Band Resonant Raman Study of 62 Isolated Single-Walled Carbon Nanotubes. *Phys. Rev. B* **2002**, *65*, 155412-1–155412-9.
30. Sze, S. M. Semiconductor Devices, Physics and Technology. In *p*−*n Junction*; John Wiley & Sons: Singapore, 1985; pp 92−95.
31. Mahan, G. D. *Many-Particle Physics*; Plenum: New York, 1990.
32. Ozel, T.; Gaur, A.; Rogers, J. A.; Shim, M. Polymer Electrolyte Gating of Carbon Nanotube Network Transistors. *Nano Lett.* **2005**, *5*, 905–911.
33. Siddons, G. P.; Merchin, D.; Back, J. H.; Jeong, J. K.; Shim, M. Highly Efficient Gating and Doping of Carbon Nanotubes with Polymer Electrolytes. *Nano Lett.* **2004**, *4*, 927–931.
34. Back, J. H.; Kim, S.; Mohammadi, S.; Shim, M. Low-Frequency Noise in Ambipolar Carbon Nanotube Transistors. *Nano Lett.* **2008**, *8*, 1090–1094.
35. Balasubramanian, K.; Fan, Y.; Burghard, M.; Kern, K. Photoelectronic Transport Imaging of Individual Semiconducting Carbon Nanotubes. *Appl. Phys. Lett.* **2004**, *84*, 2400–2402.
36. Kocabas, C.; Hur, S.-H.; Gaur, A.; Meitl, M. A.; Shim, M.; Rogers, J. A. Guided Growth of Large-Scale, Horizontally Aligned Arrays of Single-Walled Carbon Nanotubes and their Use in Thin-Film Transistors. *Small* **2005**, *1*, 1110–1116.